

# Spitzer observations of the N157B supernova remnant and its surroundings

E. R. Micelotta, B. R. Brandl, F. P. Israel

Sterrewacht Leiden, Leiden University, P.O. Box 9513, 2300 RA Leiden, The Netherlands  
e-mail: micelot@strw.leidenuniv.nl

Received 26 March 2008 / Accepted 16 February 2009

## ABSTRACT

**Aims.** We study the LMC interstellar medium in the field of the nebula N157B, which contains a supernova remnant, an OB association, ionized gas, and high-density dusty filaments in close proximity. We investigate the relative importance of shock excitation by the SNR and photo-ionization by the OB stars, as well as possible interactions between the supernova remnant and its environment. **Methods.** We apply multiwavelength mapping and photometry, along with spatially resolved infrared spectroscopy, to identifying the nature of the ISM using new infrared data from the *Spitzer* space observatory and X-ray, optical, and radio data from the literature. **Results.** The N157B SNR has no infrared counterpart. Infrared emission from the region is dominated by the compact blister-type HII region associated with 2MASS J05375027-6911071 and excited by an O8-O9 star. This object is part of an extended infrared emission region that is associated with a molecular cloud. We find only weak emission from the shock-indicator [FeII], and both the excitation and the heating of the extended cloud are dominated by photo-ionization by the early O stars of LH 99. **Conclusions.** Any possible impact by the expanding SNR does not now affect the extended cloud of molecules and dust, despite the apparent overlap of SNR X-ray emission with infrared and H $\alpha$  emission from the cloud. This implies that the supernova progenitor cannot have been more massive than about 25 M $_{\odot}$ .

**Key words.** supernova remnants – N157B – LMC – H II regions – dust – photoionization – shock-excitation

## 1. Introduction

The H $\alpha$ -emitting region N157 B (Henize 1956) in the Large Magellanic Cloud is on the southwestern fringe (projected linear distance 90 pc from the center) of the major star-forming complex 30 Doradus. In a limited area of (projected) diameter 65 pc, the field contains a supernova remnant, an OB association, HII emission regions, bubbles of low-density hot gas, as well as the neutral material in dense clouds (Lazendic et al. (2000) and references therein). The structure, dynamics, and energy balance of this region are poorly understood. There is even uncertainty about the nature of the emission observed at different wavelengths.

The OB association LH 99 (Lucke & Hodge 1970) is seen on the sky in the same direction as N157B, and is often considered to be associated with it because it has the same foreground extinction (Wang & Gotthelf 1998). LH 99 contains a large number of (early) O stars (Schild & Testor 1992), powerful ionizing sources whose strong stellar winds are expected to produce bubbles of low-density hot gas (Townesley et al. 2006) and to illuminate the dusty filaments and clouds such as the nearby molecular cloud 30Dor-22 (Johansson et al. 1998).

Much of the nebula N157 B can be identified with the Crab-like supernova remnant (SNR) B0538-691. Its embedded X-ray pulsar PSR J0537-6910 suggests an age of about 5000 yr (Marshall et al. 1998; Wang & Gotthelf 1998). The N157B radio counterpart MC 69 (Le Marne 1968; McGee et al. 1972) has a spectral index  $\alpha = -0.19$ ,  $S_{\nu} \propto \nu^{\alpha}$  (Mills et al. 1978; Lazendic et al. 2000). Such a flat spectrum is characteristic of thermal HII region emission, as well as of nonthermal Crab-type

SNR emission. However, various observations strongly support the latter interpretation: bright X-ray emission coincides with the radio source (Long & Helfand 1979), the ratio of radio-to-optical intensity is quite high (Dickel et al. 1994), spectral line images (Danziger et al. 1981) reveal filamentary structures with a high line ratio [SII]/H $\alpha \geq 0.7$ , the lines of [OI], [FeII], and [FeIII] are strong, whereas the HeI  $\lambda 4686$  Å line is weak. The SNR has a peculiar one-sided morphology, does not have a well-determined outer boundary, and exhibits bright radio/X-ray core surrounded by an extended envelope of linear size of 30 $\times$ 20 pc (Chu et al. 1992; Dickel et al. 1994; Lazendic et al. 2000), or even larger (Townesley et al. 2006) making the remnant unusually large in both radio and X-ray emission (Lazendic et al. 2000; Wang & Gotthelf 1998).

In such a complex environment, shocks from SNRs and photons from luminous stars compete as heating agents for the ISM. The conditions in and around N157B have therefore been a frequent subject of study. Several authors, e.g. Chu et al. (1992); Townesley et al. (2006); Chen et al. (2006) have concluded that the expanding SNR is presently colliding with the molecular cloud to its south. The impact of a shock front on dense cloud material should leave a signature detectable at mid-infrared (MIR) wavelengths (Oliva et al. 1999; Reach & Rho 2000). Confirmation of the proposed collision is of great interest, as it would identify an excellent source for studying the physics of ongoing dense ISM processing by shocks.

The use of infrared observations is particularly well-suited to trace physical conditions in dusty environments because of their insensitivity to extinction. In the following, we combine our *Spitzer* observations with literature data at a variety of wavelengths to study the role of the different physical compo-

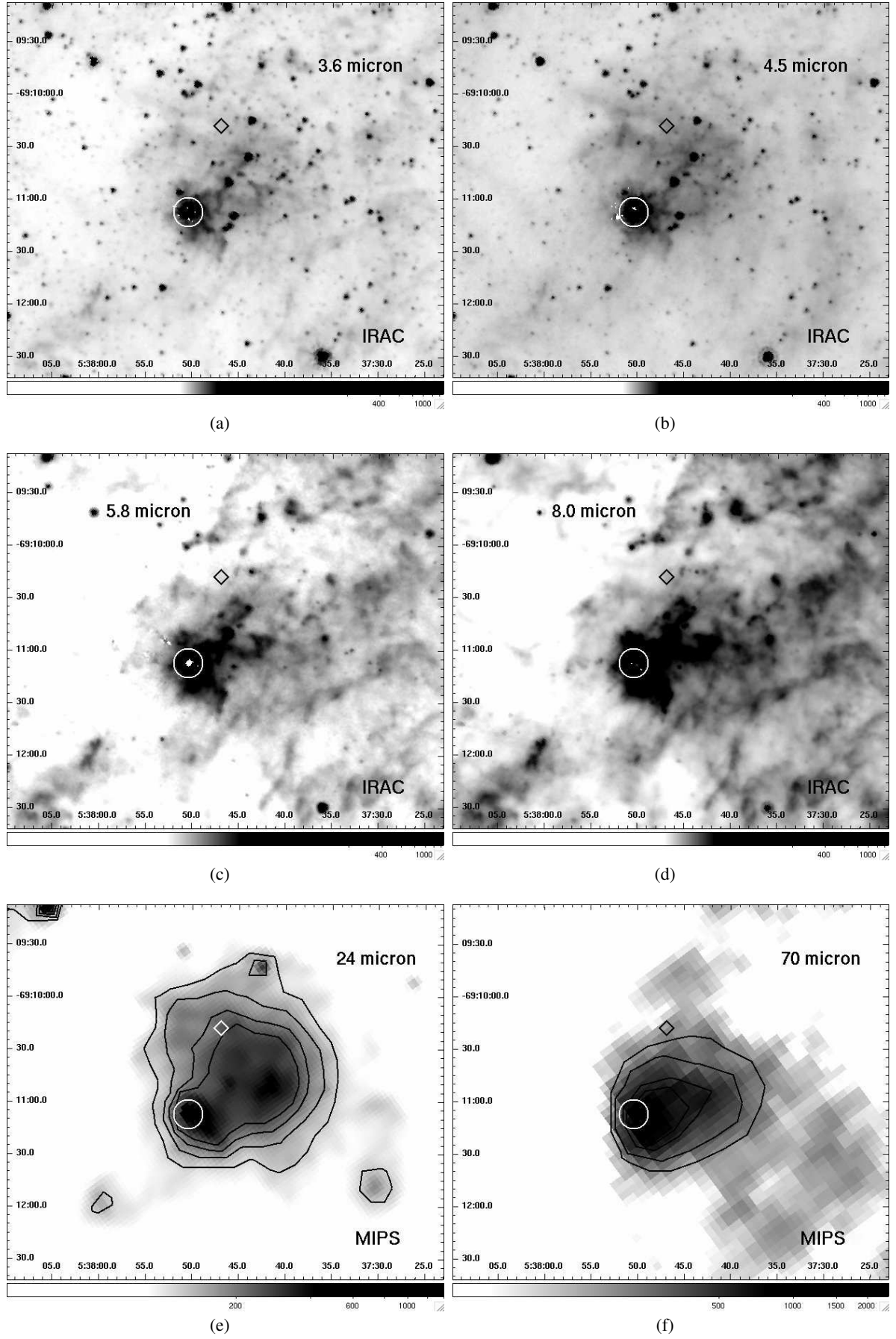


**Fig. 1.** IRAC and MIPS images of the N157B region, calibrated in MJy/sr. The diamond marks the peak of the supernova remnant X-ray emission (Sasaki et al. 2000) and the circle marks the 2MASS compact source J05375027-6911071. The coordinates are (RA, dec) J2000.

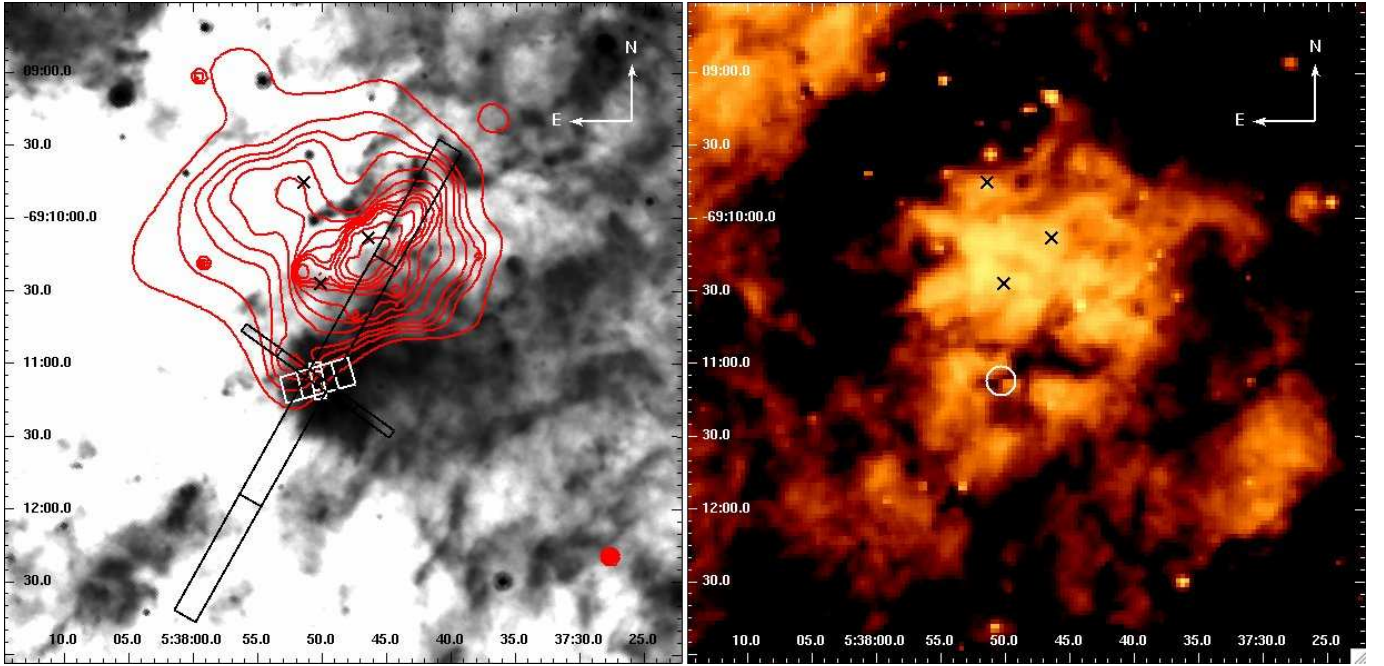


**Fig. 2.** *Left panel:* IRAC 8.0  $\mu\text{m}$  map overlaid with Chandra ACIS-S X-ray intensity contours of N157B at 4, 5, 7, 8, 12, 16, 20, 25, 30, 35, 50, 100, 500,  $30000 \times 10^{-2} \text{ counts sec}^{-1} \text{ arcsec}^{-2}$  (courtesy D. Wang). The rectangles mark the IRS slit locations: SL = east-west black, LL2 = north-south black, SH and LH are the two small white boxes in the center of the field. The O3 stars ST 1-62, 1-71, 1-78 in LH 99 ((Schild & Testor 1992)) with projected positions inside the N157B X-ray contours are marked with an “X” (Schild & Testor 1992). *Right panel:* MCELS  $H\alpha$  image of N157B (Smith & MCELS Team 1998), again with the O3 stars marked. Note the correspondence between the 8  $\mu\text{m}$  IR emission and  $H\alpha$  extinction. The compact object J05375027-6911071 is marked by a circle which also identifies the area over which we determined the  $H\alpha/[S \text{ II}]$  ratio (see Sect. 4.1). In both panels the coordinates are (RA, dec) J2000.

nents (SNR, HII region, OB association, dust clouds) and heating processes (shock-excitation, photo-ionization) in shaping the N157B region. Throughout, we adopt a distance of 50 kpc for the LMC (Westerlund 1997), so that 10'' correspond to 2.4 pc.

## 2. Observations and data processing

We have observed N157B with the Infrared Array Camera (IRAC) (Fazio et al. 2004) and with the Infrared Spectrograph (IRS) (Houck et al. 2004) on board the Spitzer Space Telescope (Werner et al. 2004), as part of the IRS guaranteed-time program (PID 63, PI J. R. Houck). The images from the Multiband Imaging Photometer for Spitzer (MIPS) have been retrieved from the archive (MIPS 24  $\mu\text{m}$ : program 3680, PI K.J. Borkowski, MIPS 70  $\mu\text{m}$ : program 20203, PI M. Meixner).

The IRAC data (Fig. 1) were taken on 7 December 2003 and consist of mosaic images in four channels at 3.6, 4.5, 5.8 and 8.0  $\mu\text{m}$ . The Basic Calibrated Data (BCD) products from the Spitzer Science Center (SSC) pipeline were used to construct the mosaic images.

The IRS spectra were taken on 26 May 2005 using the standard IRS “Staring Mode” Astronomical Observing Template (AOT). The observational setup is reported in Table 1. The IRS slit coverage is shown in Fig. 2 - left panel, outlined with rectangles: SL goes from East to West, LL2 from North to South and SH and LH are the two small rectangles in the center of the field.

Each cycle yielded two exposures at different nod positions along the slit. The data have been pre-processed by the SSC data reduction pipeline version 12.0.2 (Spitzer Observer’s Manual,

**Table 1.** IRS observational setup. The IRS modules are SL: Short-Low, LL2: Long-Low 2, SH: Short-High, LH: Long-High.

Cycles number	Duration <sup>a</sup> (sec)	IRS module	$\Delta\lambda$ ( $\mu\text{m}$ )	Resolving Power
2	14	SL	5.2 – 14.5	64 – 128
2	14	LL2	14.0 – 21.3	64 – 128
3	30	SH	9.9 – 19.6	600
3	60	LH	18.7 – 37.2	600

(a): Total integration time: SL + LL2 = 112 sec, SH + LH = 540 sec.

chapter 7<sup>1</sup>). The two-dimensional BCD constituted the basis for further processing. First we corrected the BCD frames for bad and rogue pixels with the IRSCLEAN<sup>2</sup> tool. IRSCLEAN identifies bad and rogue pixels and replaces them with the average of good nearest neighbors. Rogue pixels are single-detector pixels that show time-variable and abnormally high flux values. Next, we combined the frames from the same nod position using the mean where two frames were available, and using the median in case of three available frames. For each integration at the same position on the target, an off-source sky exposure is provided, so we computed the mean/median sky (depending again on the number of available frames) and subtracted it from the corresponding nod position frame.

Further processing was done using the SMART package version 5.5 (Higdon et al. 2004) - a suite of IDL software tools

<sup>1</sup> <http://ssc.spitzer.caltech.edu/documents/SOM>

<sup>2</sup> available at <http://ssc.spitzer.caltech.edu/archanaly/contributed/>

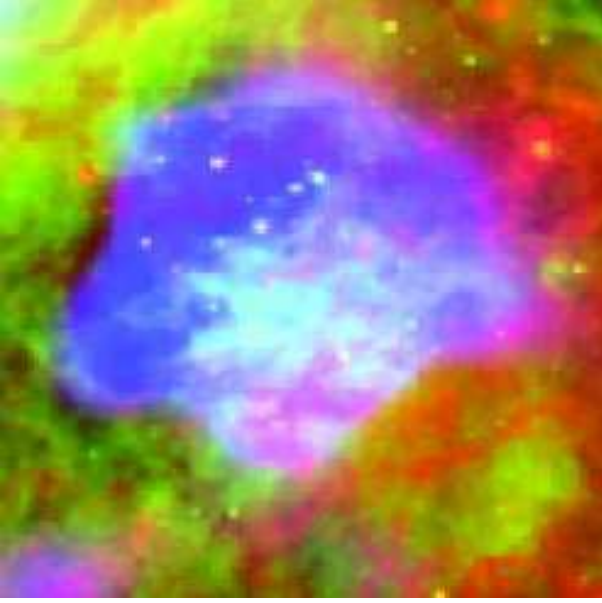


**Fig. 3.** Composite image of the N157B region: red = Spitzer IRAC 8.0  $\mu\text{m}$ , green = MCELS  $H\alpha$ , blue = Chandra \*ACIS\* 0.9 - 2.3 keV. The blue area in the center shows X-rays from the northend parts of the remnant filling a prominent hole in the 8.0  $\mu\text{m}$ . The contours of the optical and infrared emission (see Fig. 2) are recognisable in the cyan and magenta areas respectively. This picture is part of a large image of 30 Dor from Townsley et al. (2006). (Reproduced by permission of the AAS.)

**Table 2.** Infrared flux densities.

Origin	$\lambda$ ( $\mu\text{m}$ )	Bandwidth ( $\mu\text{m}$ )	Flux Density (Jy)	
			Compact Object	Extended Cloud
2MASS	1.24	0.16	$0.0013 \pm 0.0001$	—
	1.66	0.25	$0.0022 \pm 0.0002$	—
	2.16	0.26	$0.017 \pm 0.006$	—
IRAC	3.6	0.75	$0.13 \pm 0.02$	$1.7 \pm 0.3$
	4.5	1.01	$0.33 \pm 0.05$	$3.2 \pm 0.5$
	5.8	1.42	$0.66 \pm 0.1$	$7.2 \pm 1.1$
	8.0	2.93	$0.98 \pm 0.2$	$19 \pm 3.0$
MIPS	24	4.7	$1.7 \pm 0.3$	$38 \pm 6.0$
	70	19	$3.6 \pm 0.5$	$139 \pm 21.$
	160	35	$2 \pm 0.3$	$105 \pm 16.$
IRAS	12	7.0	—	$3 \pm 0.5$
	25	11.2	—	$22 \pm 3.0$
	60	32.5	—	$124 \pm 19.$
	100	31.5	—	$312 \pm 47.$

developed for spectral extraction and spectral analysis of IRS data. The high-resolution spectra were extracted using full slit extraction. The low-resolution spectra were instead extracted using SMART's interactive column extraction. The calibration is based on observations of standard stars (Decin et al. 2004). The ends of each orders, where the noise increases significantly, were manually clipped. To obtain a good match between the low and high resolution modules, the SL + LL2 spectra were scaled up by 10%. Finally the resulting spectra from the two nod positions were averaged to obtain the final spectrum shown in Fig. 4.

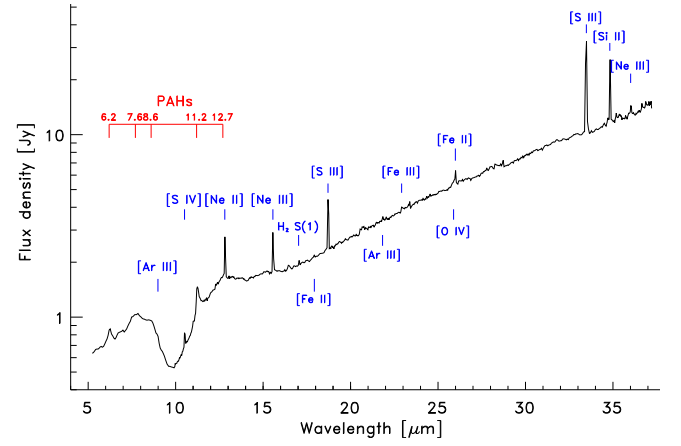


**Fig. 4.** Combined low- and high-resolution IRS spectrum of the 2MASS source J05375027-6911071.

### 3. Results and analysis

#### 3.1. IRAC and MIPS images

The IRAC and MIPS images (Fig. 1) of the N157B region are dominated by emission from the dust associated with the molecular cloud south of the X-ray emission region (peak marked by a diamond). Relatively faint in the 3.6  $\mu\text{m}$  and 4.5  $\mu\text{m}$  images, the irregularly shaped diffuse emission is quite bright at 5.8  $\mu\text{m}$ , 8.0  $\mu\text{m}$ , and 24  $\mu\text{m}$  where it appears more extended with a quasi-circular shape. In the 70  $\mu\text{m}$  image, it no longer stands out clearly as it suffers from confusion with the very extended low-surface brightness emission characteristic of the whole 30 Doradus region. The cloud is listed as object no. 1448 in the IRAS catalogue of LMC sources by Schwering (1989) and shows up in the relatively low-resolution IRAS maps as an extension of the main 30 Doradus IR source. Fig. 2 (left) and Fig. 3 show that the contour of the 8  $\mu\text{m}$  emission (sensitive to PAHs) from the cloud follows reasonably well the outline of extinction in the  $H\alpha$  image (Fig. 2 - right). Much of the infrared-emitting dust must therefore be either in front of the ionized gas, or embedded within it. From the MIPS 24  $\mu\text{m}$ , the size of the cloud is roughly 2' (28.8 pc). Its dimensions are thus similar to those of the SNR but the two are offset from one another, as shown by the superposition of the X-ray and 8  $\mu\text{m}$  maps in Fig. 2, left-hand panel. Although there is considerable overlap between the X-ray and  $H\alpha$  emission regions (Fig. 2, right-hand panel), there is no trace of an IR counterpart to the X-ray SNR emission: the two occur almost side-by-side.

The bright and compact object at RA (J2000) = 5h37m50.28s, DEC (J2000) =  $-69^\circ 11' 07.1''$  is located within the confines of the infrared cloud. In the IRAC images, it has a diameter of  $\sim 3$  pc and it is the brightest source in the field in all IRAC bands. Centimeter-wavelength radio maps by Dickel et al. (1994) and Lazendic et al. (2000) reveal weak radio emission at its position. Although there is ISO SWS and LWS spectroscopy of the extended cloud just described (Vermeij & van der Hulst 2002), the ISO apertures did not include this bright object. We have chosen this object, which is identical to the 2MASS near-IR source J05375027-6911071, as the reference position for the IRS slits (Fig. 2 - left panel).

We have collected infrared flux densities for both the compact object and the whole dust cloud shown in Fig. 1 by integrating the emission over circles with radii 6'' and 57'' centered on RA(5h37m50.3s), DEC( $-69^\circ 11' 07''$ ) and RA(5h37m45.3s), DEC( $-69^\circ 10' 47''$ ), respectively. The results are listed in Table 2,



**Table 3.** Spitzer fine-structure lines observed in J05375027-6911071.

Line ID	$\lambda_{rest}$ [ $\mu\text{m}$ ]	EP <sup>a</sup> [eV]	Flux <sup>b</sup> [ $10^{-20} \text{ W cm}^{-2}$ ]	EW <sup>a</sup> [nm]
Clear detections				
[S IV]	10.51	34.8	$2.35 \pm 0.26$	10
[Ne II]	12.81	21.6	$17.2 \pm 4.0$	80
[Ne III]	15.56	41.0	$8.4 \pm 0.26$	40
[S III]	18.71	23.3	$13.3 \pm 0.3$	60
[Fe II]	25.99	7.9	$3.32 \pm 0.93$	20
[S III]	33.48	23.3	$55.6 \pm 1.4$	210
[Si II]	34.82	8.15	$20.7 \pm 0.8$	70
[Ne III]	36.01	41.0	$1.64 \pm 0.52$	5
Marginal detections				
[Ar III]	8.99	27.6	$1.20 \pm 0.27$	4.27
H <sub>2</sub> S(1)	17.03	—	$0.8 \pm 0.37$	6.54
[Fe II]	17.93	7.9	$0.17 \pm 0.19$	1.70
[Ar III]	21.83	27.6	$0.74 \pm 0.20$	4.00
[Fe III]	22.92	16.2	$1.47 \pm 0.40$	6.53

Note. - Emission line properties obtained from single Gaussian fits in the IRS spectrum (Fig. 4).

(a): EP = Excitation Potential, EW = Equivalent Width (observed).

(b): Quoted uncertainties are the errors from the line fit and do not include calibration uncertainties.

**Table 4.** PAH dust emission features measured in J05375027-6911071.

$\lambda_{cent}^a$ [ $\mu\text{m}$ ]	Flux <sup>b</sup> [ $10^{-20} \text{ W cm}^{-2}$ ]	EW <sup>c</sup> [nm]	Relative <sup>d</sup> strength
6.2	$36.06 \pm 0.58$	34.1	1.00
7.7	$53.00 \pm 0.36$	51.5	1.47
8.6	$41.42 \pm 0.54$	40.3	1.15
11.2	$32.77 \pm 0.64$	36.7	0.90
12.7	$27.45 \pm 0.36$	26.7	0.76

(a): Central wavelength.

(b): The quoted uncertainties are the errors from the line fit and do not include the calibration uncertainties.

(c): EW = Equivalent Width (observed).

(d): Strength relative to 6.2  $\mu\text{m}$  feature.

which for convenience also yields the relevant flux densities taken from the 2MASS on-line data archive, and the IRAS database published by Schwering (1989). Although all flux-densities in Table 2 have very small formal errors, a major uncertainty (easily a factor of two) arises in the separation of the source from its surroundings. As noted by Schwering, this is clearly true for the IRAS flux densities, which are very hard to separate from the overwhelming emission of the 30 Doradus complex, but a glance at Fig. 1 shows that this problem is not limited to the IRAS data, but also extends to the Spitzer mapping of this complex region.

### 3.2. IRS Spectroscopy of J05375027-6911071

The combined high- and low-resolution spectrum of the 2MASS source J05375027-6911071 covers the wavelength range from 5  $\mu\text{m}$  to 38  $\mu\text{m}$ , and is shown in Fig. 4. The (short-wavelength)

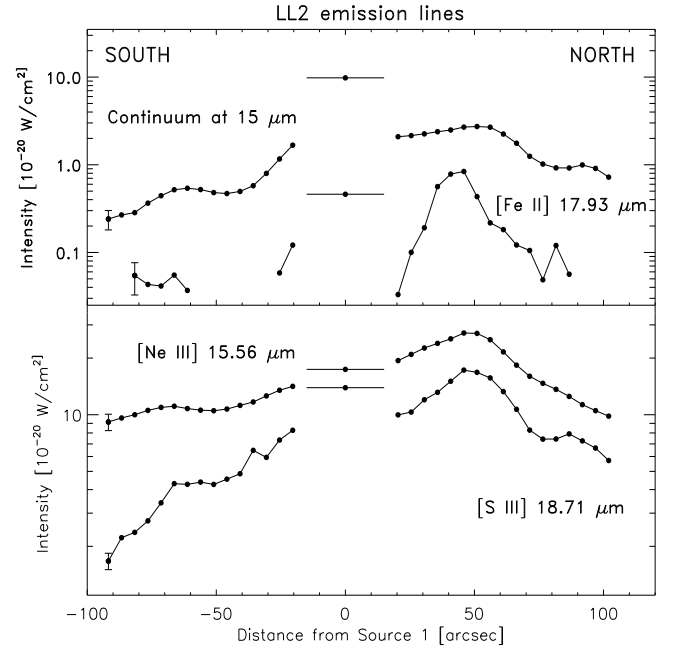


**Fig. 5.** Spatial variation of continuum and emission line intensities along the low-resolution slit LL2, calculated with the program PAHFIT. The vertical bar on the left mark indicates the representative error on fitted intensities. Spatial distances along the slit are measured from the position of J05375027-6911071 (0 arcsec). The horizontal bar indicates the size of the five-pixel wide extraction window for J05375027-6911071; all other data points refer to three-pixel wide extraction windows.

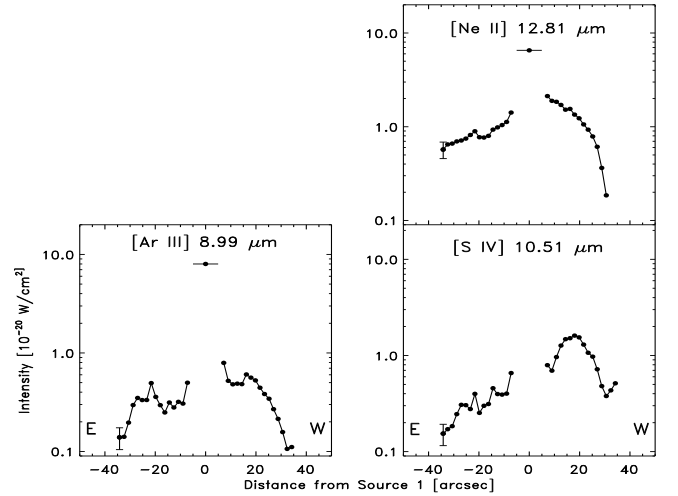


**Fig. 6.** Spatial variation of emission line intensities along the low-resolution slit SL. Otherwise as Fig. 5. Towards J05375027-6911071 the [S IV] line is undetectable because of strong silicate absorption.

low-resolution part has been extracted from the *single slit segment* centered on 2mass-j05375027-6911071 (see below), while the high resolution part results from integration over the *full length* covered by the SH and LH slits (see Fig. 2 - left-hand panel). This area includes J05375027-6911071 but also some of its fainter surroundings. As a result, the spectrum in Fig. 4 accurately reflects the emission from J05375027-6911071 shortwards of  $\sim 20 \mu\text{m}$ . However, at wavelengths beyond  $20 \mu\text{m}$  the

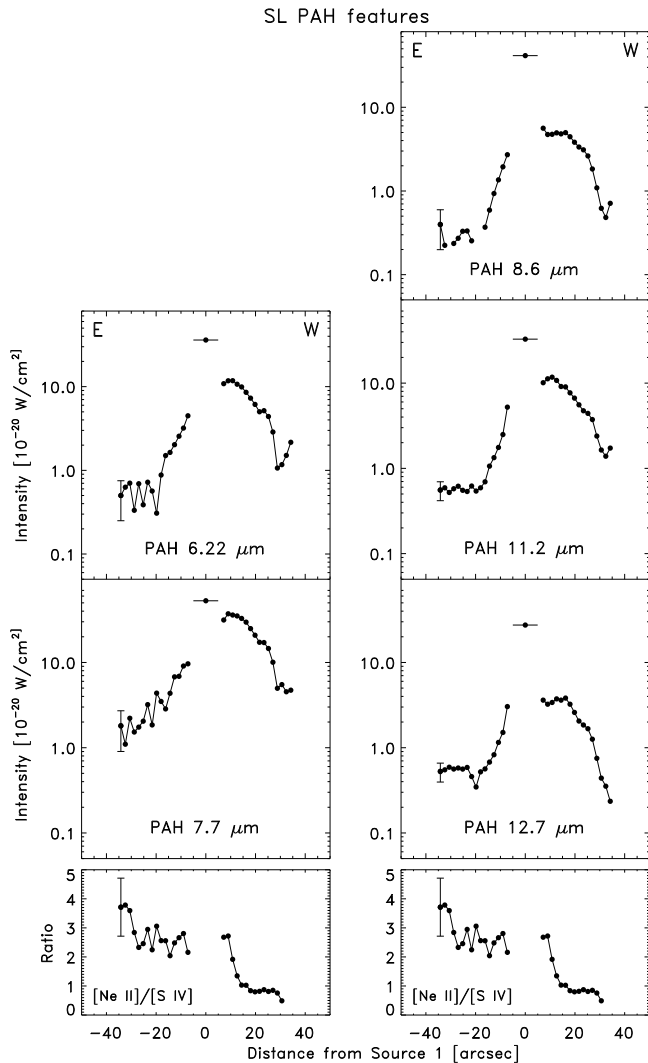


**Fig. 7.** Spatial variation of PAH feature intensities (top panels) compared to the  $[\text{Ne II}]/[\text{S IV}]$  ratio (same plot reproduced in both bottom panels for clarity) along the low-resolution slit SL. The vertical bar on the left mark indicates the representative error on fitted intensities in the region between -35 and -5 arcsec. The oscillations are due to instabilities in the fit caused by weak signals. Otherwise as Fig. 5.

spectrum includes a non-negligible contribution from the surrounding diffuse emission.

Different ISM processes have left their mark on the spectrum: emission from PAHs, absorption by silicates around  $10\ \mu\text{m}$  and in a broad band between  $15\ \mu\text{m}$  and  $22\ \mu\text{m}$ , various fine-structure emission lines and steeply increasing continuum emission from hot dust. The dust PAH features have been modelled with the program PAHFIT<sup>3</sup> (Smith et al. 2007) and the results are presented in Table 4. PAHFIT is an IDL tool for decomposing Spitzer IRS spectra, with special attention to PAH emission features, and it is primarily designed for use with Spitzer low-resolution IRS spectra. The program is based on a model consisting of starlight, thermal dust continuum with temperature from 35 to 300 K, resolved dust features and feature blends, prominent emission lines and dust extinction dominated by the silicate absorption bands at  $9.7\ \mu\text{m}$  and  $15\text{--}22\ \mu\text{m}$ . PAHFIT uses Gaussian profiles to recover the full strength of emission lines and Drude

profiles for dust emission features and blends. The fine-structure lines have been measured by single Gaussian fits within SMART, and the results are listed in Table 3. All these lines, except the iron lines, are typically associated with ionized gas in photon-dominated regions (PDRs - e.g. Martín-Hernández et al. 2002; Tielens 2005).

### 3.3. IRS spectroscopy of the extended dust cloud

As shown in Fig. 2, the SH and LH slits cover only a very limited part of the cloud, mainly the compact 2MASS object. The two much longer low-resolution slits LL2 and SL sample a much larger part of cloud, even extending into the cloud surroundings. The slits are almost perpendicular to one another and overlap at the position of the compact object 2MASS J05375027-6911071.

In order to study the spatial variation of the spectral features along the two slits, we sub-divided the region covered by each slit into 33 segments and extracted a spectrum from each segment. We have chosen overlapping extraction windows of three pixels width, moving them along the slit in single-pixel steps. Thus, adjacent extractions are not independent of one another as they overlap by two pixels. The corresponding spectrum is therefore effectively a boxcar-smoothed spectrum. These particular choices resulted from tests performed on the data to find the minimum extraction requirements needed to obtain spectra free of sampling artifacts. For the same reason, the region containing the bright object J05375027-6911071 was treated slightly differently. Here, we applied an extraction window five pixels wide, not overlapping with the adjacent pixels. As a consequence, the size of the extraction window for J05375027-6911071 exceeds the dimensions of the intersection region common to both the SL and LL2 slits; it corresponds to a  $7\text{ pc} \times 2.7\text{ pc}$  rectangle. We used PAHFIT with its default set of lines and continuum features to determine the intensities of the spectral features at every slit position. We have plotted the intensities of fine-structure emission lines and dust features thus extracted as a function of the position along the slit, expressed in terms of the distance (positive and negative) from J05375027-6911071 in Figs. 5, 6 and 7.

The SL spectra show PAH emission in the  $6.2$ ,  $7.7$ ,  $8.6$ ,  $11.2$  and  $12.7\ \mu\text{m}$  bands. In determining the intensity of the latter, we first removed the contribution from the  $[\text{Ne II}]$   $12.8\ \mu\text{m}$  line. We note that the PAH emission from the N157B region is remarkably weak compared to that of other sources in 30 Doradus (Brandl 2008).

## 4. Discussion

### 4.1. The nature of the compact object J05375027-6911071

The flux densities in Table 2 are not accurate enough to warrant detailed SED fitting of J05375027-6911071. However, by comparing various modified blackbody fits with straightforward integration we find an integrated flux of  $5 - 11 \times 10^{-13}\text{ W m}^{-2}$  which implies a luminosity  $L = 3.8 - 8.6 \times 10^4 L_{\odot}$ . This luminosity corresponds to that of a B1-O9 star if all stellar photons are converted to IR emission; it thus places a lower limit on the spectral type of the exciting star(s). Much of the emission must arise from hot dust, with temperatures between 180 and 350 K. The exciting star must therefore be close to the dense neutral material, and we would expect the interface between star and neutral material to consist of very dense ionized gas.

The Spitzer spectrum of J05375027-6911071 (Fig. 4) contains several diagnostic fine-structure lines. The  $[\text{S III}]$  lines at

<sup>3</sup> Available at <http://turtle.as.arizona.edu/jdsmith/pahfit.php>

18.7  $\mu\text{m}$  and 33.5  $\mu\text{m}$  arise from different levels with the same excitation energy and their ratio provides a measure of the electron density (e.g. Tielens 2005). We find a [SIII] 18.7  $\mu\text{m}$ / [SIII] 33.5  $\mu\text{m}$  ratio of 0.24. Collisional excitation models (Alexander et al. 1999) place this ratio in the low-density limit, and indicate the presence of an ionized gas with  $n_e \approx 100 \text{ cm}^{-3}$ . Such a density is not uncommon for a parsec-sized HII region (cf. Fig. 2 in Habing & Israel 1979). It is also quite consistent with the weak radio emission (about 40 mJy at  $\lambda\lambda 3.5\text{--}13\text{cm}$ ) in the maps published by Lazendic et al. (2000) and Dickel et al. (1994). Assuming all radio emission in this direction to be thermal and optically thin free-free emission, we calculate an r.m.s. electron density  $\langle n_e^2 \rangle^{0.5} = 100 - 250 \text{ cm}^{-3}$ . It is unlikely that the ionized gas and the hot dust have different sources of excitation. We must conclude that the bulk of the infrared line and radio continuum emission arises from gas extended over a volume much larger than occupied by the dense ionized gas surmised in the previous paragraph. As we have not resolved structure on scales less than a few parsecs, this is quite feasible.

The ratios of lines of the same species but arising from different ionization states reflect the degree of ionization and the hardness of the stellar radiation field. We have measured such pairs of neon and sulphur lines and find ratios [SIV]/[SIII] = 0.18 and [NeIII]/[NeII] = 0.49. In a sample of HII regions with different metallicities in the Milky Way, the LMC, and the SMC these two ratios are tightly correlated (cf. Fig. 1 by Martín-Hernández et al. 2002). Our result fits this correlation very well but the individual ratios are lower than those in the (very) bright LMC HII regions which have [SIV]/[SIII] = 0.6–1.0, and [NeIII]/[NeII] = 1.4–6.3. Not surprisingly, the gas in J05375027-6911071 thus has a lower degree of ionization as is expected from excitation by stars less hot than the ionizing stars in the bright LMC HII regions. The photoionization models by Schaerer & de Koter (1997) (CoStar) and by Pauldrach et al. (2001) show our line ratios to result from stellar radiation fields with  $T_{\text{eff}} = 33000\text{--}40000 \text{ K}$  corresponding to spectral type O5–O9 (cf. Martins et al. 2002). Under the same assumption of optically thin free-free radio emission, we calculate from the maps by Dickel et al. (1994) and Lazendic et al. (2000) a minimum required Lyman-continuum photon flux  $N_L = 48.96 \text{ s}^{-1}$ . This corresponds to the output of an O7.5–O9 star (Vacca et al. 1996).

Bright [FeII] 17.9  $\mu\text{m}$ , [FeII] 26.0  $\mu\text{m}$  and [SiII] 34.8  $\mu\text{m}$  lines trace the return of iron and silicon to the gas phase following the destruction of dust grains by shocks (Oliva et al. 1999; Reach & Rho 2000), but a strong [SiII] line is also frequently detected in PDRs (Peeters et al. 2002). In J05375027-6911071 [SiII] is one of the strongest detected lines, whereas the [FeII] lines are weak with respect to the others. The [SI] 25  $\mu\text{m}$  line, also expected in shocked gas (Tielens 2005), is missing but sulphur is detected as [SIII] and [SIV], a situation characteristic for photo-ionized gas.

The intensity of the optical lines [SII]  $\lambda\lambda 6717, 6731 \text{ \AA}$  and  $H\alpha$   $\lambda 6563 \text{ \AA}$  provides a reliable tool to discriminate between shock-excited and photo-ionized plasma (Long et al. 1990) and were, in fact, used to establish the nature of N157B (Danziger et al. 1981). In SNRs, [SII] emission is usually stronger than in photoionized HII regions, where sulphur is mostly doubly ionized. The value of the [S II]/ $H\alpha$  ratio separating SNRs and HII regions is about 0.4 (D’Odorico et al. 1980; Fesen et al. 1985; Long et al. 1990). No optical spectra are available for J05375027-6911071, but we may estimate the [SII]/ $H\alpha$  ratio from the MCELS line emission maps. The lines are close enough to assume that they suffer approximately the same extinction.

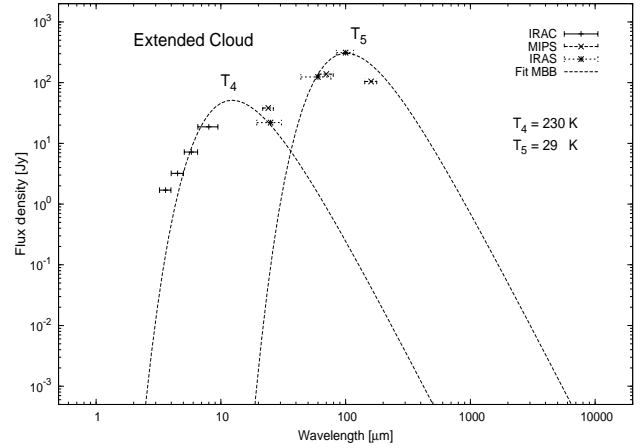


**Fig. 8.** Spectral energy distribution of infrared emission from the extended dust cloud. The data points are fitted with two modified black-body with  $T = 230$  and  $T = 29 \text{ K}$ . The horizontal bars indicate the width of the IRAC (Fazio et al. 2004), MIPS (Rieke et al. 2004) and IRAS bands (Schwering 1989). The 12  $\mu\text{m}$  IRAS point has been removed because of the strong 10  $\mu\text{m}$  silicate absorption of the compact source, which makes it impossible to separate out the extended cloud contribution.

We find a ratio [SII]/ $H\alpha = 0.2$ , which is typical for H II regions (Long et al. 1990). Note that in most of N157B, this ratio exceeds  $\sim 0.7$  (Danziger et al. 1981).

Finally, we note that the 9.7  $\mu\text{m}$  silicate absorption feature is very strong towards J05375027-6911071, with an optical depth  $\tau_{9.7} \approx 1.1$ . This implies the presence of a large column of neutral material in front of the ionized line emission region.

Thus, the 2MASS source J05375027-6911071 contains a purely photo-ionized gas of moderate density. The high column-density and elevated temperature of the dust suggests a blister-type geometry (Israel 1978) seen from the back, and a source of excitation located close to the interface of the HII region with the obscuring dense neutral material. In that case, no more than about half of the ionizing photons may escape, and we conclude from this and the local radiation field hardness that the excitation of J05375027-6911071 is caused by an obscured but no longer embedded O8 or O9 star.

#### 4.2. The northeast edge of the dust cloud

The intensity variation of the spectral features along the rather short SL slit is shown in Fig. 6 and 7. The SL slit runs from northeast to southwest. It is potentially of interest as it cuts across the X-ray SNR/IR dust cloud boundary (Fig. 2 left-hand panel). Apart from J05375027-6911071, most of the emission in all lines comes from the dust cloud, outside the X-ray contours. The [S IV] intensities peak around +15 arcsec (3.5 pc) southwest from J05375027-6911071. Towards the object itself, because of the low resolution of the SL slit we could not separate the [SIV] emission from the silicate absorption at 9.7  $\mu\text{m}$ , contrary to the high resolution spectrum where the [SIV] is well detected. Both [Ar III] and [Ne II] have intensity distributions strongly peaking on J05375027-6911071, and that of [ArIII] is almost symmetrical. The [NeII] distribution has an asymmetry similar to but less outspoken than that of [SIV]. The ion with the highest ionization potential ([SIV]) appears to trace the dust continuum best, but the lack of more extensive spectral coverage makes it very hard to draw any solid conclusions.

The various (weak) PAH features have symmetrical intensity distributions, very similar to each other (Fig. 7) and consistent with the 8.0  $\mu\text{m}$  image which shows the stronger emission in southwest of the X-ray contours. Fig. 7 also shows the [NeII]/[SIV] ratio. The excitation potentials of NeII and SIV are 21.6 and 34.8 eV respectively. The ratio of the corresponding ionic lines [NeII]/[SIV] can be used as a tracer of the hardness of the interstellar radiation field (ISRF) in a similar way as the ratio [NeII]/[NIII] (see for example Giveon et al. 2002): a lower ratio corresponds to a harder ISRF. If PAHs were destroyed by FUV photons (e.g. Madden et al. 2006), PAH intensities should be correlated with the [NeII]/[SIV] ratio.

Inspection of Fig. 7 reveals a clear trend: the PAH profiles peak where the [NeII]/[SIV] ratio dives (+20'' W) probably indicating the edge of an ionized region where PAHs are destroyed. We refer for a more extensive and detailed discussion of PAHs in the whole 30 Doradus region to Bernard-Salas (2008).

#### 4.3. Conditions in the extended dust cloud

Fig. 5 depicts the spatial intensity variation of spectral features along the significantly longer SE-NW LL2 slit. The slit extends from a region with weak IR emission and no X-rays to the northwest, fully crossing the H $\alpha$  and X-ray emitting SNR (Fig. 2 left-hand panel). The compact source J05375027-6911071 is brighter than its surroundings in the continuum, and in the [SIII] and [FeII] lines, but not in the [NeIII] line. Beyond this source, the distributions of [SIII], [NeII] and the continuum are similar and peak about 50 arcsec (12 pc projected distance) to its northwest. The [FeII] from the diffuse cloud is relatively sharply peaked. Although uncertain, this peak may indicate the presence of shocked gas at an SNR/dust cloud interface. As the Ne[III] and [SIII] intensity distributions peak closest to the early O stars in LH 99 (see Fig. 2 and Sec. 4.3), they seem to reflect the radiative effects of these.

The ISO SWS and LWS instruments have provided spectroscopy from differently-sized regions (Vermeij et al. 2002) roughly covering the O3 stars marked in Fig. 2. The LL2 slit misses the SWS aperture completely, but does overlap with part of the LWS aperture. The [NeIII] 15.6/36.0  $\mu\text{m}$ , [SIII] 18.7/33.5  $\mu\text{m}$ , and [OIII] 51.8/88.4  $\mu\text{m}$  ratios (6.73, 0.40, 0.56 resp.) are all in the low-density limit, indicating  $n_e \leq 100 \text{ cm}^{-3}$ . The ISO spectra also show [FeII] 26.0  $\mu\text{m}$  and [SiII] 34.8  $\mu\text{m}$  line emission but not sufficiently dominant to be ascribed unequivocally to shock excitation. More importantly, the ISO data by Vermeij et al. (2002) imply ratios [SIV]/[SIII] = 0.25 and [NeIII]/[NeII] = 1.74. These values are also in excellent agreement with the relation established by Martín-Hernández et al. (2002), and place the cloud somewhat closer to the bright LMC nebulae. Although there are complications briefly discussed by Martín-Hernández et al. (2002), the ratios, taken at face value, suggest excitation by O5-O6 stars rather than by O3 stars.

The spectral energy distribution of the extended infrared cloud is shown in Fig. 8. The emission peak is consistent with a modified black-body of temperature  $T = 29 \text{ K}$  ( $B(\nu, T) \propto \nu^\beta$ , with  $\beta = 2$ ). Integration of the emission yields a flux of  $1.1 - 1.5 \times 10^{-11} \text{ W m}^{-2}$  implying a luminosity  $L = 0.8 - 1.1 \times 10^6 L_\odot$ . There is a second hot dust component, with a temperature  $T \approx 230 \text{ K}$ , and a luminosity (excluding emission from J05375027-6911071)  $L = 4 - 5 \times 10^5 L_\odot$ . In the 12  $\mu\text{m}$  IRAS band the compact source has a strong silicate absorption at 10  $\mu\text{m}$ , which makes not possible the separation of the compact source and extended cloud contributions. Before fitting the hot dust component we thus removed the 12  $\mu\text{m}$  IRAS point, for

which the flux density is in fact 30 times lower than for the neighboring bands. Because of the very strong temperature dependence of dust emissivity, the mass in the hot dust component represents only a minute fraction of the total mass. The three O3 stars dominating the LH 99 population are projected onto the northeastern edge of the infrared cloud as depicted at 24  $\mu\text{m}$  in Fig. 1. To their southwest, i.e. closer to the brightest part of the nebula, there are at least 2 O5 stars, 5 O6 stars, and 5 O7 stars (cf. Schild & Testor 1992). Using the luminosity scale by Vacca et al. (1996), we find that these stars add another  $L(\text{O5-O7}) = 4.1 \times 10^6 L_\odot$  to the luminosity  $L(\text{O3}) = 3.6 \times 10^6 L_\odot$  already provided by the brightest stars. The hardness of the resulting mean radiation field should therefore not be very different from the one estimated above.

Emission from the radio source appears to avoid the dark cloud (see Fig. 4 in Dickel et al. 1994). This is not expected if the dust cloud is only a foreground object, and it therefore indicates physical contact between the radio (SNR) and infrared (molecular cloud) sources respectively. However, the infrared cloud reradiates at most 15% of the total photon output of the association members, requiring it to cover only about a steradian as seen from the average O star. LH 99 should thus be deemed to be quite capable of providing the energy to power the infrared cloud, and there seems to be no need to invoke energy inputs provided by an SNR impact.

Chu et al. (1992) have suggested that no more than about 20% of the radio emission from MC 69 is thermal in origin, so that  $S_{5\text{GHz}}(th) \leq 0.45 \text{ Jy}$  (cf. Lazendic et al. 2000). This requires a maximum Lyman continuum photon flux  $N_L \leq 1.0 \times 10^{50} \text{ s}^{-1}$ . The three somewhat excentric O3 stars provide a combined flux  $N_L = 2.5 \times 10^{50} \text{ s}^{-1}$ , and the more embedded later-type O stars an almost equal  $N_L = 2.4 \times 10^{50} \text{ s}^{-1}$ . Thus, the UV photon flux likewise should be sufficient to provide for the ionization of the HII nebula associated with the SNR and dust cloud.

#### 4.4. The SNR revisited

The actual location of the cloud with respect to the remnant is still poorly determined. The data presented here have revealed no evidence for shocked material, although the dense cloud of dust and molecules does appear to be quite close to the SNR. Is the absence of such impact (shock) signatures consistent with the dynamical evolution of the remnant? We assume that the remnant expansion is in the Sedov phase (Wang & Gottlieb 1998), so that the temporal evolution of the spherical blast wave with radius  $R_S$ , produced by the supernova explosion into a medium of uniform density  $\rho_0$ , is described by (Sedov 1959; McCray & Snow 1979):

$$R_S = 1.15 (E_0/\rho_0)^{1/5} t^{2/5} \approx 13 (E_{51}/n_0)^{1/5} t_4^{2/5} \text{ pc.}$$

We assume an initial energy  $E_{51} = E_0/(10^{51} \text{ erg s}^{-1}) = 1$ , a remnant age  $t_4 = t/(10^4 \text{ yr}) = 0.5$  (Marshall et al. 1998), and a remnant radius  $R_S \approx 15 \text{ pc}$  (Chu et al. 1992; Dickel et al. 1994; Lazendic et al. 2000; Chen et al. 2006). Thus, the present size of the supernova remnant requires an initial density of no more than  $n_0 = 0.12 \text{ cm}^{-3}$ . This rules out the possibility of N157B having expanded into an interstellar gas cloud of any significant density, and confirms the notion that expansion occurred inside a wind-blown cavity cleared out by the supernova progenitor (Chu et al. 1992). In their X-ray study of 30 Doradus and N157B, Townsley et al. (2006) present a composite X-ray/H $\alpha$ /mid-IR image (their Fig. 14) that indeed shows a shell of ionized gas and warm dust surrounding the SNR. To verify whether a suitable low-density cavity could have been generated by the supernova progenitor,



we calculate its expected size by (McCray & Snow 1979, and references therein):

$$R_S \approx 27 L_{36}^{1/5} n_0^{-1/5} t_6^{3/5} \text{ pc}$$

where  $R_S$  is the cavity radius,  $L_{36}$  the constant wind luminosity in units of  $10^{36} \text{ erg s}^{-1}$ ,  $n_0$  the ambient gas particle density in  $\text{cm}^{-3}$ , and  $t_6$  the time that the wind has been blowing in millions of years. The wind luminosity  $L_{36}$  is given by:  $L_{36} \approx 0.3(M_*/20M_\odot)^{2.3} \text{ erg s}^{-1}$ . We adopt a  $M_* = 25 M_\odot$  (corresponding to an O8–O9 star), intermediate between the values predicted by the Thielemann et al. (1996), Heger et al. (2003) and Woosley & Weaver (1995) models so that  $L_{36} = 0.5$ . The relevant time  $t_6 = 3.2$  is the entire lifetime of the progenitor, derived from e.g. Karttunen (1995):  $t \sim (M_*/M_\odot)^{-2.5} \times 10^{10} \text{ yr}$ . The observed radius  $R_S$  of about 15 pc implies an average density of  $n_0 = 310 \text{ cm}^{-3}$  for the ambient medium into which the windblown shell has expanded. Such a value is compatible with the densities of a few hundred per cc that we estimated in the previous section for the clouds in the region. Even the larger radius  $R_S \approx 22 \text{ pc}$  gleaned from Townsley et al. (2006) can be accommodated as it still yields  $n_0 = 50 \text{ cm}^{-3}$ . This situation changes rapidly, however, if we consider a more massive supernova progenitor. For instance, for  $M_* = 50 M_\odot$  and  $R_S = 15 \text{ pc}$  we have  $L_{36} = 2.5$  and  $t_6 = 0.6$ , and find an average ambient density of only  $n_0 = 9 \text{ cm}^{-3}$ .

Thus, we conclude that the lack of clear indications for an SNR impact on the dust cloud seen in the IRAC and MIPS images is consistent with the supernova explosion of a moderately massive star. Only now would the SNR expanding in the cavity begin to overtake the windblown shell produced by the star over its lifetime. The apparent lack of shocks is not easily reconcilable with a supernova progenitor as massive as the presently most luminous members of the LH 99 association. This confirms an independent conclusion by Chen et al. (2006) that the progenitor should have been in the narrow mass range  $M = 20 - 25 M_\odot$ .

## 5. Conclusions

From an analysis of Spitzer photometric mapping and spectroscopy of the SNR-dominated region N157B in the LMC, we find that:

- There is no evidence of an infrared counterpart to the supernova remnant in the IRAC and MIPS images.
- The infrared emission is dominated by a cloud of dust and molecular gas adjacent to the remnant, containing the compact 2MASS source J05375027-6911071.
- The object J05375027-6911071 has a diameter of about 3 pc, an electron-density of  $100\text{--}250 \text{ cm}^{-3}$ , and is photo-ionized by an O8–O9 star. It is probably an open HII blister structure, seen from the back.
- In spite of the projected overlap between the SNR X-ray emission and the infrared cloud, there is at best very marginal evidence of shocked gas, while almost all data suggest photo-ionization and photon-heating to be the mechanisms dominating the infrared cloud.
- The extended dust cloud is associated with ionized emission of a density of typically  $100 \text{ cm}^{-3}$ , presumably at the edges of a denser molecular cloud. As the extended dust reradiates only about 10 per cent of the luminosity of the 15 brightest and nearby O stars in the LH 99 OB association, these stars are sufficient to explain the heating of the dust cloud.
- The absence of clear evidence of shocks implies that at present the molecular/dust cloud is not significantly im-

pacted by the remnant. This suggests that the supernova progenitor was a moderately massive star of mass  $M \approx 25 M_\odot$ .

**Acknowledgements.** We gratefully acknowledge D. Wang, J. Dickel, and R. Gruendl for providing Chandra data, radio continuum observations, and information on the N157B stellar population, and we would like to thank the referee for careful reading and useful comments. E.R.M. thanks A. Jones and A. Tielens for support and useful discussions and acknowledges financial support by the EARA Training Network (EU grant MEST-CT-2004-504604). This work is based in part on observations made with the *Spitzer Space Telescope*, which is operated by the Jet Propulsion Laboratory, California Institute of Technology, under NASA contract 1047.

## References

- Alexander, T., Sturm, E., Lutz, D., et al. 1999, *ApJ*, 512, 204  
 Bernard-Salas, J. 2008, in preparation  
 Brandl, B. R. 2008, in preparation  
 Chen, Y., Wang, Q. D., Gotthelf, E. V., et al. 2006, *ApJ*, 651, 237  
 Chu, Y.-H., Kennicutt, Jr., R. C., Schommer, R. A., & Laff, J. 1992, *AJ*, 103, 1545  
 Danziger, I. J., Goss, W. M., Murdin, P., Clark, D. H., & Boksenberg, A. 1981, *MNRAS*, 195, 33P  
 Decin, L., Morris, P. W., Appleton, P. N., et al. 2004, *ApJS*, 154, 408  
 Dickel, J. R., Milne, D. K., Kennicutt, R. C., Chu, Y.-H., & Schommer, R. A. 1994, *AJ*, 107, 1067  
 D’Odorico, S., Dopita, M. A., & Benvenuti, P. 1980, *A&AS*, 40, 67  
 Fazio, G. G., Hora, J. L., Allen, L. E., et al. 2004, *ApJS*, 154, 10  
 Fesen, R. A., Blair, W. P., & Kirshner, R. P. 1985, *ApJ*, 292, 29  
 Giveon, U., Sternberg, A., Lutz, D., Feuchtgruber, H., & Pauldrach, A. W. A. 2002, *ApJ*, 566, 880  
 Habing, H. J. & Israel, F. P. 1979, *ARA&A*, 17, 345  
 Heger, A., Fryer, C. L., Woosley, S. E., Langer, N., & Hartmann, D. H. 2003, *ApJ*, 591, 288  
 Henize, K. G. 1956, *ApJS*, 2, 315  
 Higdon, S. J. U., Devost, D., Higdon, J. L., et al. 2004, *PASP*, 116, 975  
 Houck, J. R., Roellig, T. L., van Cleve, J., et al. 2004, *ApJS*, 154, 18  
 Israel, F. P. 1978, *A&A*, 70, 769  
 Johansson, L. E. B., Greve, A., Booth, R. S., et al. 1998, *A&A*, 331, 857  
 Karttunen, H. 1995, *Fundamental Astronomy* (Springer)  
 Lazendic, J. S., Dickel, J. R., Haynes, R. F., Jones, P. A., & White, G. L. 2000, *ApJ*, 540, 808  
 Le Marne, A. E. 1968, *MNRAS*, 139, 461  
 Long, K. S., Blair, W. P., Kirshner, R. P., & Winkler, P. F. 1990, *ApJS*, 72, 61  
 Long, K. S. & Helfand, D. J. 1979, *ApJ*, 234, L77  
 Lucke, P. B. & Hodge, P. W. 1970, *AJ*, 75, 171  
 Madden, S. C., Galliano, F., Jones, A. P., & Sauvage, M. 2006, *A&A*, 446, 877  
 Marshall, F. E., Gotthelf, E. V., Zhang, W., Middleditch, J., & Wang, Q. D. 1998, *ApJ*, 499, L179+  
 Martín-Hernández, N. L., Vermeij, R., Tielens, A. G. G. M., van der Hulst, J. M., & Peeters, E. 2002, *A&A*, 389, 286  
 Martins, F., Schaerer, D., & Hillier, D. J. 2002, *A&A*, 382, 999  
 McCray, R. & Snow, Jr., T. P. 1979, *ARA&A*, 17, 213  
 McGee, R. X., Brooks, J. W., & Batchelor, R. A. 1972, *Australian Journal of Physics*, 25, 581  
 Mills, B. Y., Turtle, A. J., & Watkinson, A. 1978, *MNRAS*, 185, 263  
 Oliva, E., Moorwood, A. F. M., Drapatz, S., Lutz, D., & Sturm, E. 1999, *A&A*, 343, 943  
 Pauldrach, A. W. A., Hoffmann, T. L., & Lennon, M. 2001, *A&A*, 375, 161  
 Peeters, E., Martín-Hernández, N. L., Damour, F., et al. 2002, *A&A*, 381, 571  
 Reach, W. T. & Rho, J. 2000, *ApJ*, 544, 843  
 Rieke, G. H., Young, E. T., Engelbracht, C. W., et al. 2004, *ApJS*, 154, 25  
 Sasaki, M., Haberl, F., & Pietsch, W. 2000, *A&AS*, 143, 391  
 Schaerer, D. & de Koter, A. 1997, *A&A*, 322, 598  
 Schild, H. & Testor, G. 1992, *A&AS*, 92, 729  
 Schwering, P. B. W. 1989, *A&AS*, 79, 105  
 Sedov, L. 1959, *Similarity and Dimensional Methods in Mechanics* (New York: Academic)  
 Smith, J. D. T., Draine, B. T., Dale, D. A., et al. 2007, *ApJ*, 656, 770  
 Smith, R. C. & MCELS Team. 1998, *Publications of the Astronomical Society of Australia*, 15, 163  
 Thielemann, F.-K., Nomoto, K., & Hashimoto, M.-A. 1996, *ApJ*, 460, 408  
 Tielens, A. G. G. M. 2005, *The Physics and Chemistry of the Interstellar Medium* (University of Cambridge Press)  
 Townsley, L. K., Broos, P. S., Feigelson, E. D., et al. 2006, *AJ*, 131, 2140  
 Vacca, W. D., Garmany, C. D., & Shull, J. M. 1996, *ApJ*, 460, 914

- Vermeij, R., Damour, F., van der Hulst, J. M., & Baluteau, J.-. P. 2002, A&A, 390, 649
- Vermeij, R. & van der Hulst, J. M. 2002, A&A, 391, 1081
- Wang, Q. D. & Gotthelf, E. V. 1998, ApJ, 494, 623
- Werner, M. W., Roellig, T. L., Low, F. J., et al. 2004, ApJS, 154, 1
- Westerlund, B. E. 1997, The Magellanic Clouds (University of Cambridge Press)
- Woosley, S. E. & Weaver, T. A. 1995, ApJS, 101, 181

## List of Objects

- ‘N157 B’ on page 1
- ‘30 Doradus’ on page 1
- ‘LH 99’ on page 1
- ‘PSR J0537-6910’ on page 1
- ‘J05375027-6911071’ on page 4